


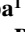







Mercury's Exosphere as Seen by BepiColombo/PHEBUS Visible Channels During the First Two Flybys



Key Points:

- PHEBUS observed Mercury's extended exosphere of calcium on the morning side beyond ~10,000 km
- The observed calcium profiles may be explained by the 2D effects of altitude and local time
- Additional species were detected, potentially manganese and potassium

R. Robidel^{1,2} , E. Quémerais¹ , J. Y. Chaufray¹ , D. Koutroumpa¹ , F. Leblanc¹ , A. Reberac¹, I. Yoshikawa³, K. Yoshioka³ , G. Murakami⁴ , O. Korablev⁵ , D. Belyaev⁵ , M. G. Pelizzo⁶, and A. J. Corso⁷

¹LATMOS-IPSL, CNRS, UVSQ, Paris-Saclay, Sorbonne Université, Guyancourt, France, ²European Space Agency, ESAC, Madrid, Spain, ³Tokyo University, Tokyo, Japan, ⁴Institute of Space and Astronautical Science, Japan Aerospace Exploration Agency, Sagami-hara, Japan, ⁵IKI, Moscow, Russia, ⁶Department of Information Engineering, University of Padova, Padova, Italy, ⁷National Research Council of Italy, Institute of Photonics and Nanotechnologies, Padova, Italy

Correspondence to:

R. Robidel,
rozenn.robidel@latmos.ipl.fr

Citation:

Robidel, R., Quémerais, E., Chaufray, J. Y., Koutroumpa, D., Leblanc, F., Reberac, A., et al. (2023). Mercury's exosphere as seen by BepiColombo/PHEBUS visible channels during the first two flybys. *Journal of Geophysical Research: Planets*, 128, e2023JE007808. <https://doi.org/10.1029/2023JE007808>

Received 24 MAR 2023
 Accepted 7 DEC 2023

Author Contributions:

Conceptualization: R. Robidel, E. Quémerais, J. Y. Chaufray, D. Koutroumpa, F. Leblanc
Data curation: R. Robidel, A. Reberac
Formal analysis: R. Robidel, E. Quémerais, J. Y. Chaufray
Funding acquisition: E. Quémerais
Investigation: R. Robidel, E. Quémerais
Methodology: R. Robidel, E. Quémerais
Software: R. Robidel, E. Quémerais, A. Reberac
Supervision: R. Robidel, E. Quémerais
Validation: R. Robidel, E. Quémerais
Visualization: R. Robidel
Writing – original draft: R. Robidel, E. Quémerais
Writing – review & editing: E. Quémerais, J. Y. Chaufray, D. Koutroumpa, F. Leblanc, A. Reberac, I. Yoshikawa, K. Yoshioka, G. Murakami, O. Korablev, D. Belyaev, M. G. Pelizzo, A. J. Corso

© 2023 The Authors.

This is an open access article under the terms of the [Creative Commons Attribution-NonCommercial License](https://creativecommons.org/licenses/by-nc/4.0/), which permits use, distribution and reproduction in any medium, provided the original work is properly cited and is not used for commercial purposes.

Abstract BepiColombo, the ESA/JAXA joint mission performed its first flyby of Mercury on 1 October 2021 and its second on 23 June 2022. PHEBUS observed the exosphere of Mercury during these flybys notably with its visible channels c404 (centered on the potassium emission line at 404 nm) and c422 (centered on the calcium emission line at 422 nm). The c422 signal shows not only an enhancement of calcium (Ca) near the dawn region but also a very extensive Ca exosphere on the morning side beyond 10,000 km. The e-folding distance deduced from our Ca profiles (2,500–2,800 km) is in agreement with the value reported by MESSENGER at similar true anomaly angles. We use a Chamberlain model to determine the temperature and density at the exobase. Using the morning side low-altitude data, we derived a high temperature at the exobase (>50,000 K), in agreement with the MESSENGER results. We also report a day/night asymmetry in the Ca exosphere that could indicate that the source of Ca is predominantly on the dayside or be the consequence of a shift of the main source of Ca away from the dawn region. The c404 channel detected additional species at low altitudes on the morning side during both flybys. Comparison with previous studies is inconclusive and further analysis will be necessary to identify the species. Nevertheless, we can note that the e-folding distance deduced from our profile is relatively small (135 km) and that the Chamberlain model applied to our profiles seems to indicate a temperature at the exobase <3,000 K.

Plain Language Summary BepiColombo, the ESA/JAXA joint mission on its way to Mercury, has already flown over the planet twice in October 2021 and June 2022. PHEBUS (Probing of Hermean Exosphere By Ultraviolet Spectroscopy), the UV spectrometer onboard the spacecraft, observed Mercury's exosphere during the flybys at the closest parts of approach to the planet with its two visible channels notably. Mercury is surrounded by a tenuous collisionless atmosphere (exosphere) that contains a variety of species. We report the detection of exospheric calcium with an enhancement near the dawn region. We show that the calcium exosphere is much extended on the morning side, beyond 10,000 km. The observations also reveal a day/night asymmetry of the calcium exosphere. Furthermore, we report the detection of additional species. However, the flyby data alone do not allow us to formally identify the species.

1. Introduction

Launched on 20 October 2018, BepiColombo is on a 7-year journey to Mercury. It is a joint mission between the European Space Agency (ESA) and the Japan Aerospace Exploration Agency (JAXA). It comprises two spacecraft, the ESA-led spacecraft Mercury Planetary Orbiter (MPO) and the JAXA-led spacecraft Mercury Magnetospheric Orbiter (MMO). The orbiters are currently in cruise configuration that is, they are stacked on the Mercury Transfer Module (MTM). PHEBUS, standing for Probing of Hermean Environment By Ultraviolet Spectroscopy, is one of the 11 instruments on board MPO. PHEBUS is composed of two detectors operating in overlapping spectral ranges in the ultraviolet (EUV: 55–155 nm, and FUV: 145–315 nm) and two visible channels dedicated to the calcium (c422: 422 nm) and potassium (c404: 404 nm) line measurements. The instrument is devoted to the study of the exosphere of Mercury, its composition, dynamics, variability and its interface with the surface of the planet and the solar wind. The instrument and its scientific objectives are described in more detail in Chassefière et al. (2010) and Quémerais et al. (2020).

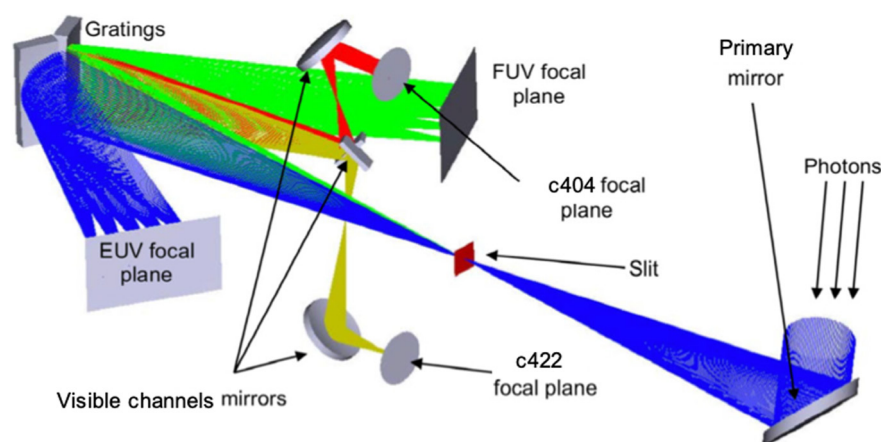


Figure 1. PHEBUS optical layout adapted from Quémerais et al. (2020).

Mercury is the only planet in our solar system not to possess substantial atmosphere. The surface-bounded exosphere of Mercury is composed almost entirely of atoms rather than molecules. Hydrogen and helium were the first neutral species to be measured by Mariner 10 Ultraviolet Spectrometer (Broadfoot et al., 1976). The potential detection of oxygen during Mariner 10 flybys was never confirmed. The Mercury Atmospheric and Surface Composition Spectrometer (MASCS) instrument on board the M_Ercury Surface, Space E_Nvironment, G_Eochemistry, and Ranging (M_ESS_ENGER) spacecraft regularly searched for oxygen throughout the orbital mission but could not detect it. Sodium and potassium (K) were the next neutral species detected in Mercury's exosphere. They were discovered with ground-based telescopes (Potter & Morgan, 1985, 1986), as was the calcium (Bida et al., 2000). During the three Mercury flybys, M_ESS_ENGER/MASCS yielded detections of magnesium (Mg) (McClintock et al., 2009) and ionized calcium (Ca⁺) (Vervack et al., 2010). During its orbital phase, M_ESS_ENGER conducted near-daily observations of exospheric Mg (Merkel et al., 2017). Bida and Killen (2011) reported first-time detections of aluminum (Al) and iron (Fe) by ground-based observations. Fe was not observed by M_ESS_ENGER/MASCS, but the detection of Al was confirmed by M_ESS_ENGER/MASCS observations during the orbital phase (Vervack et al., 2016). The same observations yielded the first detection of manganese (Mn) and confirmed the detection of Ca⁺. To generate and maintain the exosphere, several processes act at Mercury. The exosphere is supplied both by incoming sources (e.g., solar wind, meteoroids ...) and by particles released from the surface through different processes (Wurz et al., 2022). The major release processes include thermal desorption, photon- and electron-stimulated desorption, impact vaporization and sputtering (Killen et al., 2018). These source processes are balanced by loss processes such as photoionization, gravitational escape, or acceleration by solar radiation pressure to escape velocity.

On 1 October 2021 and 23 June 2022, BepiColombo performed flybys of Mercury. During both flybys, PHEBUS operated its visible channels, along with the EUV detector for the first flyby and the FUV detector for the second flyby, at the closest parts of the approach to the planet. Here we report the results of the visible channels, the detection of exospheric Ca emission line at 422.7 nm, and the potential detection of K doublet at 404 nm and Mn triplet at 403 nm.

This study aims to present the PHEBUS visible channel data acquired during the first two flybys of Mercury and to provide a preliminary qualitative comparison with the M_ESS_ENGER results. We start with a brief description of the instrument. Then, in a second section, we analyze the data from both flybys. In a third section, we compare these results to those of M_ESS_ENGER. In a fourth section, we use the Chamberlain model to fit our data. Finally, we discuss the results in the last section.

2. Instrument's Description

The PHEBUS instrument design is described in Chassefière et al. (2010) and Quémerais et al. (2020). Here, we concentrate on the details that will be used in the following sections. The optical design is shown in Figure 1.

Photons from the observed source enter the baffle and reach the primary mirror. The photons are then focused on the slit at the focal plane of the primary mirror. Then, they reach one of the two holographic gratings that share

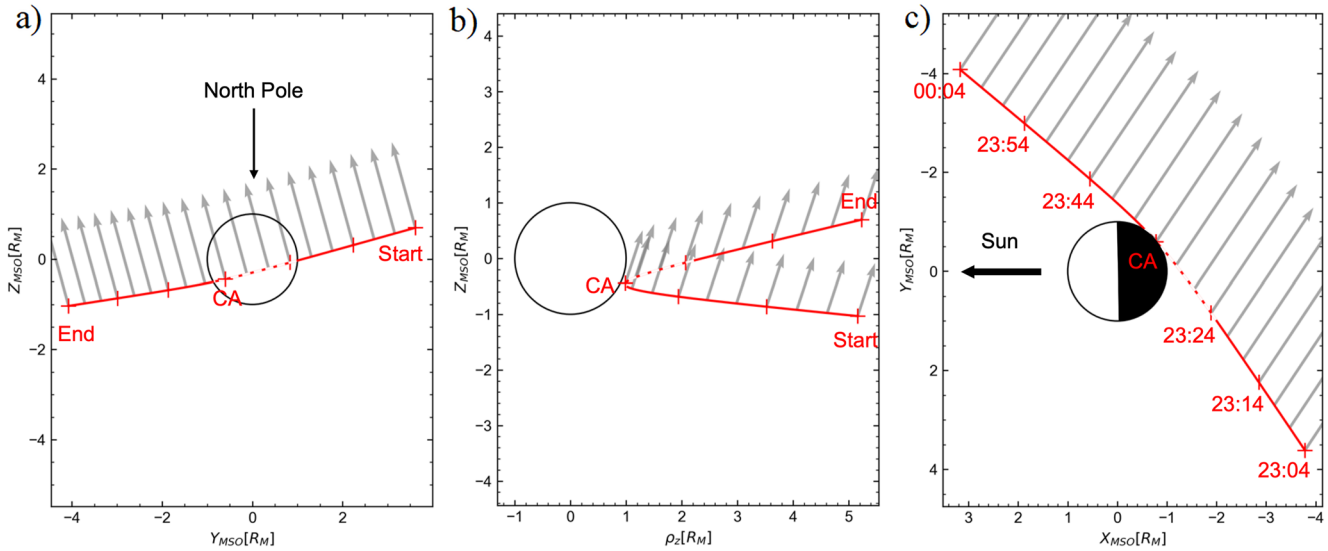


Figure 2. BepiColombo first Mercury flyby as seen (a) from the Sun, (b) in a Z – ρ – Z plane in the MSO reference frame and (c) looking down on Mercury's orbit plane. The black circle represents the planet, the gray arrows the boresight of PHEBUS FoV and the red line the spacecraft trajectory. The red dotted line represents the transit in Mercury's shadow.

the pupil. By design, photons measured by the two visible channels (c404 and c422) are reflected by the FUV grating and are caught by two mirrors positioned at spots corresponding to the 404 and 422 nm wavelengths. The separation between the two mirrors is large enough so that we would expect that there is no cross-talk between the two channels for photons scattered by the FUV gratings. However, visible photons are also scattered by the EUV grating and the positions of the mirrors allow photons at 422 nm to be caught by the mirror of c404. This is why there could be a small contamination of the c404 channel by the Ca emission.

The slit that defines the size of the field of view (FoV) is mounted on a mechanism and can be removed. When the slit is removed, the field of view is defined by the entrance pupil at the end of the baffle (closest to the primary mirror). By removing the slit, we can increase the solid angle of the instrument by a factor 20, which means that the count rate on an extended source increases by the same factor. It also decreases the spectral resolution for an extended source by a factor 10.

3. Data From the First and Second Flybys of Mercury

3.1. Mercury Swing-By 1 (MSB1)

The first flyby of Mercury by BepiColombo occurred on 1 October 2021. The spacecraft arrived on the planet's nightside, crossed its shadow and then moved to its dayside (Figure 2). The closest approach (CA) to the surface took place at 23:34 UTC at an altitude of ~ 200 km, a few minutes before the spacecraft crossed the terminator. Figure 2 represents the geometry of the first flyby of Mercury in the BepiColombo Mercury-centric Solar Orbital (MSO) frame. The MSO coordinate system is defined by the x -axis pointing from Mercury toward the Sun, the y -axis being perpendicular to the x -axis and opposite to the direction of Mercury's orbital velocity and the z -axis completing the right-handed system, pointing northward.

The PHEBUS instrument was switched in 30 min before closest approach. The observation sequence lasted for 1 hour. The slit was removed to increase the signal to noise ratio. The sampling frequency was 10 s. The integration time for each individual measurement was 8 s, the remaining 2 s being used by the instrument to process the detector images and transmit them to the spacecraft. During the whole observation, three channels were activated: the two visible channels at 404 and 422 nm and the EUV detector. Additional parameters related to the flyby are listed in Table 1.

The visible channel count rate profiles yield several important insights (Figure 3a). First, they clearly indicate the observation geometry of the flyby, the transit in the shadow of Mercury in particular, and the maximum of

Table 1

Relevant Parameters for the Flybys of Mercury (CA = Time of the Closest Approach, TAA = True Anomaly Angle, r = Heliocentric Distance, dr/dt = Mercury's Radial Velocity Relative to the Sun)

Flyby n°	CA [UTC]	TAA [°]	r [AU]	dr/dt [km.s ⁻¹]	Sun-target-observer angle [°]	Local solar time	(β, λ)
1	2021-10-01T23:34:42Z	262.6	0.381	-9.97	136	02:29:19	(69°, 18°)
2	2022-06-23T09:44:22Z	264.8	0.378	-10.02	122	03:44:18	(74°, 343°)

Note. (β, λ) corresponds to the ecliptic latitude and longitude of the center of the FoV of PHEBUS. All values are given at the time of the closest approach.

the emission on the morning side after the CA. The maximum is reached shortly after the exit of the spacecraft from the shadow of Mercury as, even though the spacecraft is illuminated, a part of the line of sight still remains in the shadow of Mercury. Then, as the spacecraft moves away from Mercury, the count rate of both channels decreases. Note that both signals are polluted by unexpected sporadic spikes. They occur when the spacecraft is out of the eclipse on the morning side. The spikes affect both channels at the exact same time with the same magnitude, suggesting that they are related to the light reflected on particles (e.g., outgassed particles). Moreover, these spikes did not affect the EUV detector.

In spite of these spikes, the c422 profile strongly points to the detection of the emission line of calcium at 422.8 nm and shows an enhancement near the dawn region. The Ca exosphere appears to be very extensive on the morning side as we still have some signal at the end of the observation on the c422 channel at ~10,000 km of altitude.

As for the c404 channel, the signal is less intense and more confined. Because the signal is very polluted by the sporadic spikes, it is difficult to know if it reflects the detection of species. The channel having a wide bandwidth (Appendix A) is able to detect the doublet of K at 404 nm, the triplet of Mn at 403 nm, two Al emission lines (394.51 and 396.26 nm) and two Ca⁺ emission lines (393.48 and 396.96 nm). However, it is impossible to distinguish the contribution of each species as the signal is integrated over the bandwidth.

3.2. Mercury Swing-By 2 (MSB2)

The second flyby occurred on 23 June 2022. The geometry of observation was similar to the first flyby: the spacecraft arrived on the planet's nightside, crossed its shadow and then moved to its dayside (Figure 4). The closest approach took place at 09:44 UTC, about 200 km above Mercury's surface (Table 1). The observation sequence changed between the first and the second flybys. The instrument was switched on 1 hour before the closest approach and observed for half an hour only with the visible channels. Then, the FUV detector was switched on along with the visible channels for 50 min of observation.

As with the first flyby, the count rate profiles of the visible channels indicate the observation geometry of the flyby; the transit in the shadow of Mercury and the maximum of the emission on the morning side after the CA

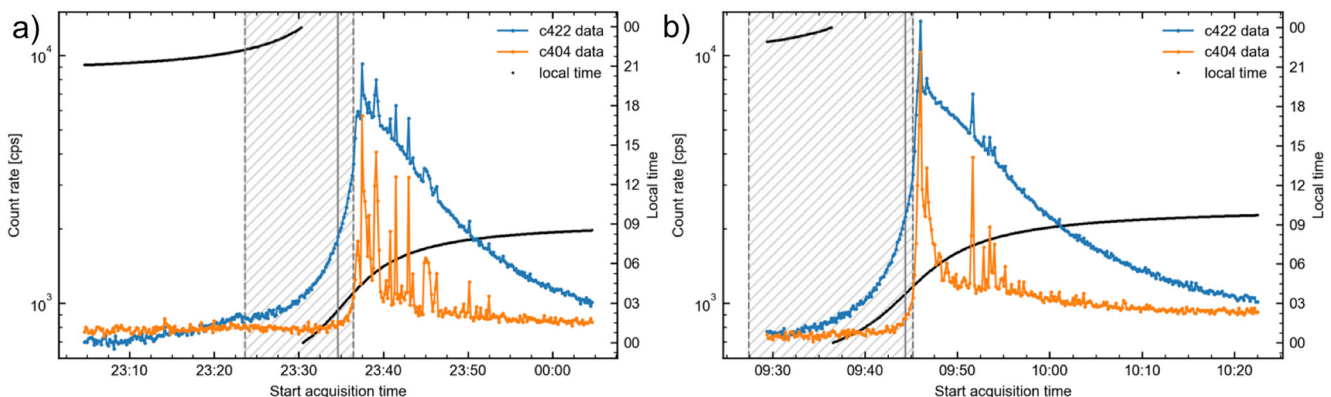


Figure 3. c404 (orange curve) and c422 (blue curve) count rate as a function of the time during MSB1 (left panel) and MSB2 (right panel). The black dots represent the local time. The gray-hatched area corresponds to the transit in the shadow of Mercury. The solid gray line represents the closest approach.

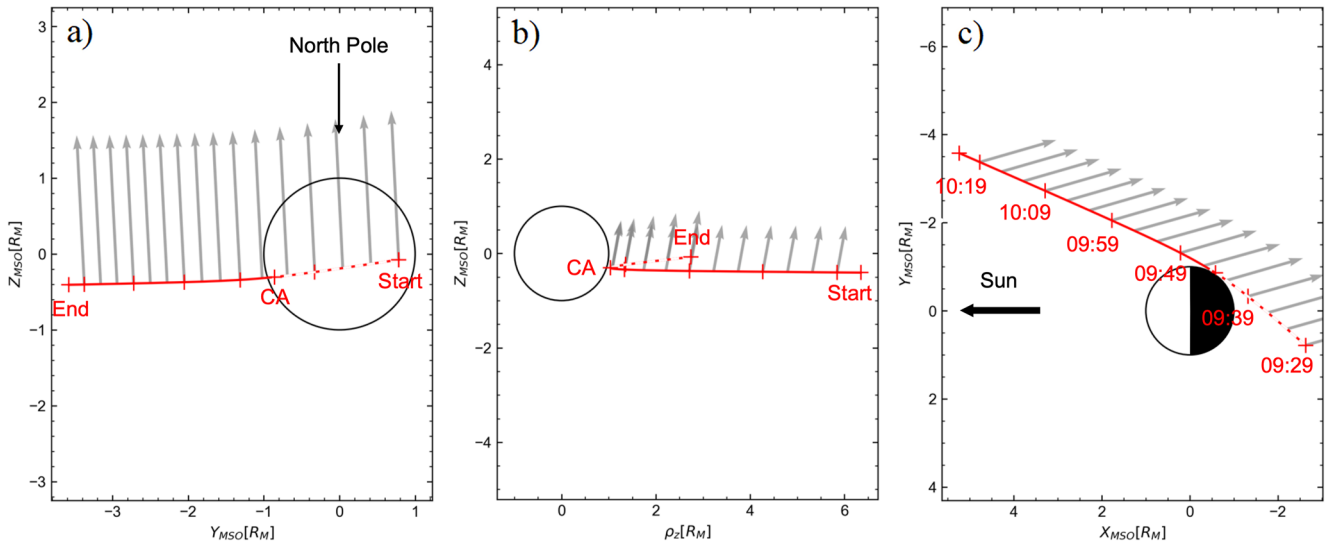


Figure 4. BepiColombo second Mercury flyby as seen (a) from the Sun, (b) in a Z – ρ Z plane in the MSO reference frame and (c) looking down on Mercury's orbit plane. The black circle represents the planet, the gray arrows the boresight of PHEBUS FoV and the red line the spacecraft trajectory. The red dotted line represents the transit in Mercury's shadow.

(Figure 3b). Calcium was again detected with the c422 channel, confirming the extent of the Ca exosphere on the morning side up to $\sim 13,000$ km. Again, we note multiple spikes on top of the general emission profile once out of the planet's shadow. Their occurrence is nevertheless less frequent than during MSB1, which allows to notice that the c404 and c422 signals are different. The c404 data clearly reflect the detection of additional species at low altitudes on the morning side, which was not obvious during the first flyby.

4. Comparison of BepiColombo Results During Flybys With MESSENGER Observations

4.1. Calcium

Calcium was first detected in the exosphere of Mercury from the ground (Bida et al., 2000; Killen et al., 2005) through its emission line at 422.7 nm. MESSENGER/MASCS also observed this emission line during its three Mercury flybys (McClintock et al., 2008, 2009; Vervack et al., 2010). These flybys revealed a dawn/dusk asymmetry and an energetic calcium source. Indeed, Vervack et al. (2010) reported high e-folding values over the poles (1,878 km in the north and 1,621 km in the south). The analysis made by Burger et al. (2012) produced similar e-folding values ($1,840 \pm 140$ km and $1,716 \pm 200$ km). A more complete view of the calcium exosphere was derived from the orbital observations in Burger et al. (2014):

- The e-folding distance is approximately constant over a Mercury year,
- There is a strong seasonal variation in the surface radiance at dawn,
- There is very little year-to-year variability in the surface radiance,
- There is a strong dawn/dusk asymmetry with a peak at dawn.

To compare our results with MESSENGER's, we converted the count rate to brightness, knowing that:

$$CR = I \times A_{\text{eff}} \times \Omega \quad (1)$$

With CR, the count rate corrected for the background (s^{-1}), I the brightness ($\text{s}^{-1} \cdot \text{cm}^{-2} \cdot \text{sr}^{-1}$), A_{eff} the effective area of the detector (cm^2) and Ω the solid angle (sr). We corrected the count rate for different contributions: the dark current (inherent to the detector), the zodiacal light (i.e., sunlight reflected by interplanetary dust) and the stellar contribution. During both flybys, the spacecraft was kept in an inertial attitude, PHEBUS pointing toward the ecliptic North. No (or very few) bright stars in the visible range are located in these regions, so the stellar contribution was considered negligible or at least constant throughout the flybys. Based on Leinert et al. (1998) and the calibration of the detectors, we estimated the contribution of the zodiacal light to ~ 50 counts per second

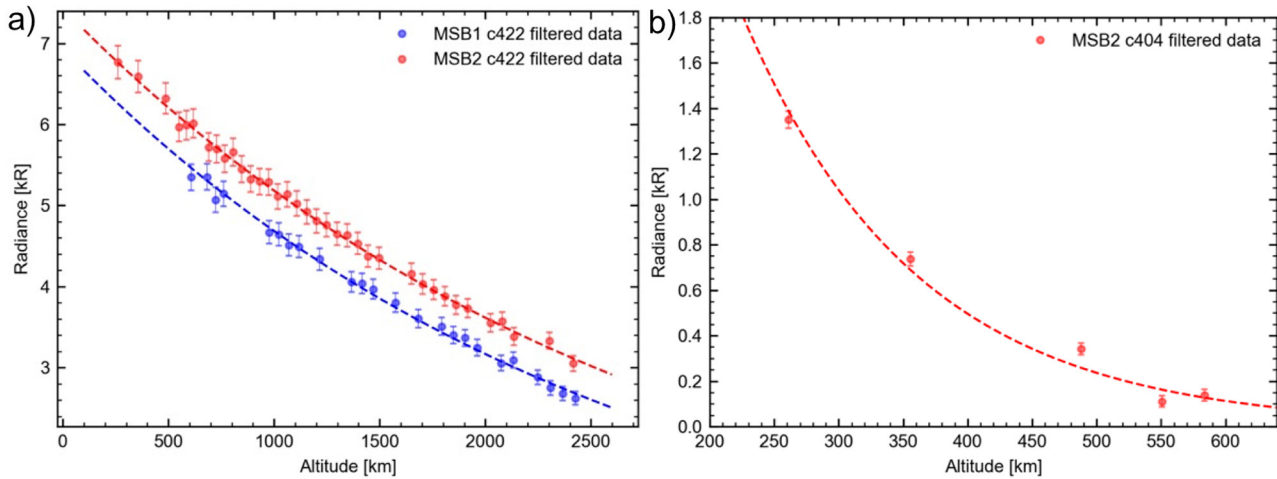


Figure 5. c422 emission profiles on the dawn side during MSB1 and MSB2 (left panel). c404 emission profiles on the dawn side during MSB2 (right panel). Exponential fits to the data are shown by the dotted lines. The dots correspond to the data that were considered to derive the exponential fits. The error bars represent the $\pm 1\sigma$ uncertainty.

at the ecliptic poles and ~ 100 counts per second at the ecliptic equator. Most of the background level is then due to the dark current. A detailed explanation of the correction is provided in Appendix B. The radiance I_R , expressed in Rayleigh, is related to brightness I as follows:

$$I_R = \frac{4\pi}{10^6} \times I \quad (2)$$

The effective area of the visible channels has been computed in flight (see Appendix A for detailed calculations): $1.19 \times 10^{-2} \pm 2.3 \times 10^{-4} \text{ cm}^2$ for c404 and $0.96 \times 10^{-2} \pm 2.8 \times 10^{-4} \text{ cm}^2$ for c422. The effective area remains the same whether the slit is across or removed; only the solid angle Ω varies. The estimation of the solid angle, performed on ground, is equal to 4.157 deg^2 when the slit is removed and 0.182 deg^2 when the slit is across.

To compare our results with MESSENGER's, we used the data from the morning side with an altitude $< 1R_M$ (Figure 5a), excluding the spikes. For the first flyby, it was difficult to use data below ~ 500 km as they are affected by the spikes. We thus used data starting at ~ 600 km for the first flyby, whereas for the second flyby, we used data starting at ~ 260 km. We derived an exponential fit to these data:

$$f(z) = f_0 e^{-z/H} \quad (3)$$

Where f_0 is the radiance at the surface, z is the altitude above the surface and H is the e -folding distance (i.e., the altitude change required for the radiance to drop by a factor e).

Table 2 summarizes the derived parameters of the exponential fit for both flybys. The values are quite consistent from one flyby to another. This empirical analysis conducted on MESSENGER's orbital phase data gives radiance at the surface of 9 kR for the TAAs of BepiColombo's flybys and an e -folding distance between 1,500 and 2,000 km (Burger et al., 2014). The slight difference could be related to the data set (flyby vs. orbit data). Burger et al. (2014) used MESSENGER data from the orbital phase. The orbit of MESSENGER was highly elliptical and MESSENGER observed the exosphere only when it was far from the orbit, between 6,000 and 12,000 km. Their line of sight was therefore crossing the entire exosphere, whereas in flyby, as the spacecraft is already in the exosphere, the line of sight only covers a limited part of the exosphere.

Table 2
Derived Values of the Exponential Fit to c422 and c404 Data

Channel	Flyby n°	f_0 [kR]	H [km]
c404	2	9.60 ± 0.65	135 ± 3
c422	1	6.93 ± 0.26	$2,555 \pm 142$
	2	7.43 ± 0.21	$2,777 \pm 145$

4.2. Potassium, Manganese, Aluminum, and Singly Ionized Calcium

Potassium has been observed in Mercury's exosphere with ground-based telescopes via emission from its D lines at 766.49 and 769.89 nm. Unfortunately, these two strong resonance lines were outside the spectral range of MESSENGER/MASCS. Attempts to detect the K emission lines at 404.48

and 404.52 nm were not successful. Only an upper limit of a few Rayleighs was derived (Vervack et al., 2016). In contrast, using ground-based observations at 769.9 nm, Lierle et al. (2022) estimated the disk-averaged brightness for the K doublet at 404 nm at 50 R. They also reported the enhancement of exospheric K at low to midlatitudes and a north-south asymmetry, with the strongest emission in the south.

Singly ionized calcium was first detected in Mercury's exosphere during the third MESSENGER flyby (Vervack et al., 2010). The ions were observed at approximately $1\text{--}2 R_M$ antisunward of the planet and mostly near the equatorial plane. Vervack et al. (2016) confirmed the presence of Ca^+ in Mercury's exosphere with the observations of two lines at 393.48 and 396.96 nm.

Bida and Killen (2011, 2017) reported ground-based measurements of aluminum via its emission line at 396.2 nm. Vervack et al. (2016) confirmed the presence of Al in Mercury's exosphere with the clear measurement of two emission lines at 394.51 and 396.26 nm with MESSENGER/MASCS.

Manganese was unexpectedly detected by MESSENGER/MASCS through its emission triplet at 403 nm (403.19, 403.42, and 403.56 nm) (Vervack et al., 2016).

Ca^+ (while in orbit), Al and Mn were detected only toward the end of the mission, confined to a small region (predawn nightside region) and a limited range of Mercury season (TAA between 0° and 70°). The location and timing of these detections correspond to the intersection of Mercury with the comet Encke dust trail. Killen and Hahn (2015) indeed proposed this correlation to explain the spike in the Ca emission source rate observed over similar true anomaly angles. The three species could then come from Encke dust impacting the dawn side of Mercury. But the observed Mn profile is far different from those of Al and Ca^+ , which could indicate that Mn perhaps derives from the cometary dust rather than the surface of the planet itself. However, the Al profile observed by MESSENGER is quite different from that observed from the ground. In the ground-based observations (Bida & Killen, 2017), Al shows an exponential decrease, consistent with a hot exosphere, whereas the MESSENGER observations (Vervack et al., 2016) showed that Al may exhibit a flat to increasing profile with altitude. Note that the observations of Al do not cover the same altitude ranges (860–2,100 km for ground-based observations and 250–650 km for MESSENGER observations).

To compare our results with MESSENGER's, we converted the count rate to brightness. For the c422 channel, we corrected the data for the background (i.e., dark current, zodiacal light and stellar contributions). Note that an additional correction is to be considered for the c404 channel: the Ca cross-talk. A detailed description of the correction is provided in Appendix B. To derive the exponential fit, we considered the c404 low-altitude data on the morning side (altitude <600 km). Unfortunately, the data from the first flyby were too much affected by the spikes; we then considered the second flyby only (Figure 5b). We also excluded the spikes to derive the exponential fit. The e-folding distance we derived is relatively small (Table 2), indicating a low-energy source process.

Among the species reported by Vervack et al. (2016), only the Mn profile shows an exponential decrease with the altitude. This is why we derived an exponential fit to this Mn profile, giving radiance at the surface of 0.95 kR and an e-folding distance of ~ 100 km. The e-folding distance is consistent with the one derived from c404 data during the second flyby but not the radiance at the surface. Moreover, BepiColombo flybys of Mercury were performed at TAAs quite different from those for which the detection of Mn is reported (Table 1). Furthermore, during both BepiColombo flybys of Mercury, the detection was not confined to the predawn nightside region (local times around 2–5 a.m.), but extends from ~ 4 to 6 a.m. that is, toward the dawn-morning side region.

We could not compare the profiles observed by PHEBUS to a potassium profile from MESSENGER since it did not detect this emission line.

5. Chamberlain Model

The empirical approach of the previous section (exponential fit on the intensities) allowed us to compare our results with those of MESSENGER. In this section, we take a physical approach using the Chamberlain exospheric model (Chamberlain, 1963) with a fit on the densities. We start by recalling the different assumptions of this model before applying it to the PHEBUS data acquired during the Mercury flybys.

5.1. Theory

Chamberlain's exospheric model (Chamberlain, 1963) is a 1D spherical model whose main assumptions are:

- Maxwellian velocity distributions at the exobase,
- Complete absence of collisions above the exobase,
- Stationary distribution functions in the exosphere,
- The only force acting on the particles is the gravity force.

The model allows us to determine the velocity distribution function at any point of the exosphere by solving the Liouville equation. The density is obtained by integrating this function on all the allowed trajectories. The density n is written in the form:

$$n(r) = n_0 e^{-(U-U_0)/kT} \zeta(U/kT) \quad (4)$$

$$U(r) = \frac{GmM}{r} \quad (5)$$

With n_0 the density at the exobase, U the gravitational potential energy of a particle of mass m , U_0 the potential energy at the exobase, k the Boltzmann constant, T the temperature at the exobase, G the gravitational constant, M the planetary mass and r the height. The partition function ζ is the sum of three terms (ζ_{bal} , ζ_{esc} and ζ_{sat}) which describe the three types of possible trajectories of exospheric particles:

1. Ballistic orbits—the ballistic particles come from the exobase but their energy is insufficient to allow them to escape. Their trajectory will be elliptical.
2. Escaping orbits—the escaping particles come from the exobase and have a sufficient energy to escape the attraction of the planet. Their trajectory is hyperbolic.
3. Satellite orbits—the satellite particles do not come from the exobase but are in orbit around the planet.

Because the exobase occurs at the surface of Mercury, collisions between atoms in the exosphere are improbable; therefore, only the ballistic and escaping partitions were considered.

Chamberlain's theory shows some limitations when applied to Mercury's exosphere. First, Mercury's exosphere is not spherically symmetric. Then, several processes are known to deplete Mercury's exosphere (e.g., surface sticking, ionization followed by transport along magnetic lines, Jeans escape and acceleration by radiation pressure), but only Jeans escape is considered in Chamberlain's theory. Finally, the model considers gravity as the only force acting on the particles, but we know that some atoms are accelerated by solar radiation pressure. However, the effect of radiation pressure on neutrals is small at low altitudes. Moreover, "Radiation acceleration has the greatest effect on the motion of Na atoms and is not much of a factor when determining the motion of Mg atoms because of weak absorptions. For Ca, the trajectories are affected, although the short photoionization lifetime [...] results in a large fraction of Ca atoms being photoionized before radiation acceleration effects become significant." (Killen et al., 2018).

Despite its limitations, Chamberlain's model provides a simple analytic description of the exosphere that requires only two independent parameters: the temperature and density at the exobase.

5.2. Application to the c422 Profiles

Previous works, based on ground- or space-based observations, have indicated high-temperature calcium. From linewidth measurements, Bida et al. (2000) and Killen et al. (2005) derived a temperature between 12,000 K and 20,000 K. More recently, Burger et al. (2012, 2014) determined the Ca distribution to be consistent with a temperature of ~50,000–70,000 K. Therefore, we tested several temperatures (Figure 6). For both flybys, we computed the associated illuminated column density N (i.e., the integrated density n along the illuminated part of the line of sight) for each line of sight and each tested temperature T . We then derived the radiance I_R (R) from

$$I_R = 10^{-6} gN \quad (6)$$

Where g is the photon scattering coefficient, also known as the excitation rate, that is, the number of photons one atom scatters per unit time (s^{-1}), N is the illuminated column density of the atoms along the line of sight (cm^{-2}). The g -value can be derived as

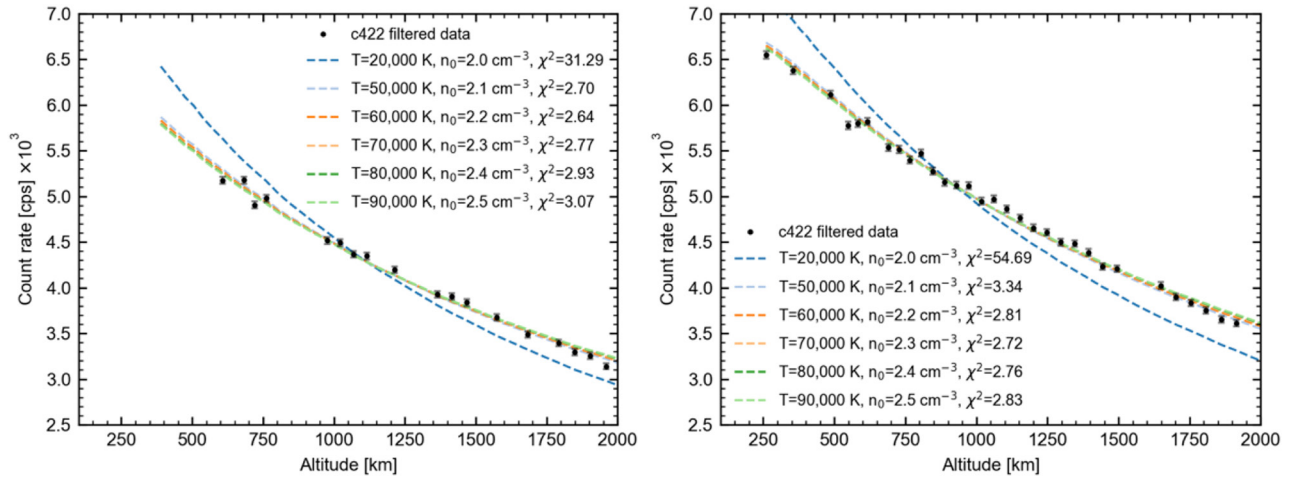


Figure 6. Ca Chamberlain model fits to low-altitude c422 data on the dawn side during MSB1 (left panel) and MSB2 (right panel). The dashed lines represent Chamberlain models at different temperatures. The temperatures along with their corresponding density and χ^2 error estimate are included in the right-hand corner of each panel. The error bars represent the 1σ uncertainties.

$$g = \frac{F_\lambda}{r^2} \frac{\lambda^2}{c} \frac{\pi e^2}{m_e c} f \quad (7)$$

Where F_λ is the solar flux at the radiation wavelength λ at 1AU from the Sun, r is the distance from the Sun, c is the speed of light, e is the electron charge, m_e is the electron mass and f is the oscillator strength factor related to the transition probability. For the computations, we used the high-resolution solar spectrum TSIS-1 Hybrid Solar Reference Spectrum (Coddington et al., 2021) and retrieved the values of the oscillator strength factor from the NIST database (Kramida et al., 2022). The g -value has been computed for the species according to the radial velocity of Mercury with respect to the Sun and the heliocentric distance of the observation corresponding to the flybys (Table 1). The assumption that the atoms are at rest relative to Mercury introduces a systematic error that is negligible at the TAAs of the flybys. The oscillator strength, atomic mass and g -values are summarized in Table 3.

For each temperature, we have computed the corresponding estimate of the goodness of fit χ^2 :

$$\chi^2 = \frac{1}{n_m} \sum_i \frac{(d_i - m_i)^2}{\sigma_i^2} \quad (8)$$

Where n_m is the number of measurements, d_i is the observed value associated with the i th measurement, m_i is the modeled value associated with the i th measurement and σ_i is the uncertainty associated with each measurement. Refer to Appendix C for the computation of the uncertainties.

We first focused on the morning side data. We could not fit the profile with a single set of parameters (n_0 , T) of the Chamberlain model. This is likely due to the ionization that is not considered in the Chamberlain model. For Ca, the ionization becomes important in depleting the exosphere at a distance r_{ion} , defined as follows (Chamberlain, 1963, Equation 124):

$$\frac{r_{\text{ion}}}{r_0} = \left(\frac{3v_{\text{esc}}(r_0)\tau_{\text{ion}}}{2r_0} \right)^{2/3}$$

Where $r_0 = R_M$ is the radial distance from the center of the planet, $v_{\text{esc}}(r_0) = (2GM/r_0)^{1/2}$ is the escape velocity at the exobase and τ_{ion} is the Ca photoionization lifetime. For the Ca photoionization lifetime, we considered the value derived from Verner and co-workers cross-section (Killen et al., 2018) for the TAA corresponding to the BepiColombo flybys. For the first two flybys, $r_{\text{ion}} \cong 3R_M$, therefore the ionization becomes important at

Table 3

Parameters Used for the Chamberlain Model

Species	Wavelength in vacuum [nm]	Oscillator strength	Atomic mass [u]	g MSB1 [ph.s ⁻¹]	g MSB2 [ph.s ⁻¹]
Ca	422.792	1.75×10^0	40.078	17.69	17.97
	403.190	5.50×10^{-2}	54.93805	0.713	0.725
	403.421	4.03×10^{-2}		0.702	0.714
K	403.563	2.57×10^{-2}		0.845	0.859
	404.528	5.67×10^{-3}	39.0983	0.243	0.247
	404.835	2.63×10^{-3}		0.082	0.083

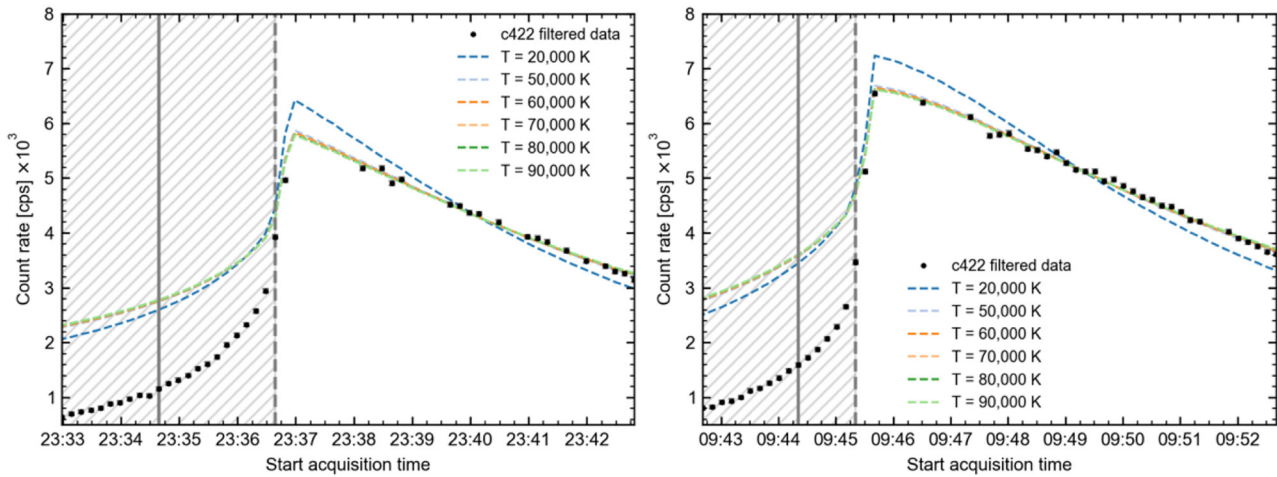


Figure 7. c422 count rate as a function of time during MSB1 (left panel) and MSB2 (right panel). The colored dashed lines represent Ca Chamberlain models at different temperatures. The solid gray line represents the CA and the hatched area represents the time spent by the spacecraft in the shadow of Mercury.

~5,000 km of altitude. We thus considered the data at low altitudes only and applied the Chamberlain model. The derived density, as well as the temperature are consistent from one flyby to another. The upper bound of the exobase temperature is not well constrained: the profiles are equally well approximated by a Chamberlain model at temperatures above 50,000 K (Figure 6). It is consistent with the temperature derived by Burger et al. (2012, 2014).

For both flybys, we noticed that the parameters of the Chamberlain model deduced from the low-altitude data on the dawn side did not fit the low-altitude data on the nightside (Figure 7), revealing a day/night asymmetry.

We then tested different temperatures with Chamberlain's model on the nightside data at low altitudes (Figure 8). The best-fit we obtained is with a temperature at the exobase of 5,500 K (resp. 6,000 K) for MSB1 (resp. MSB2), hence ~10 times lower than on the dawn side. On the other hand, densities are higher at night. The temperatures are in good agreement from one flyby to the other but not the densities (Figure 8).

5.3. Application to the c404 Profiles

Regarding the c404 channel, we focused on the morning side data at low altitudes where we detected species and considered the second flyby only (same as for the exponential fit, see Section 4.2). We have tested two species with the Chamberlain model that is, K and Mn, and several temperatures for each species. Note that

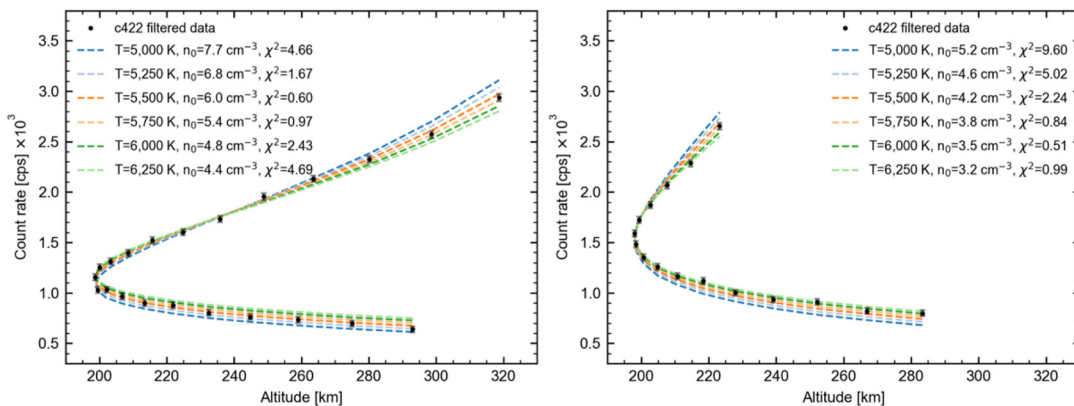


Figure 8. Ca Chamberlain model fits to low-altitude c422 data on the nightside during MSB1 (left panel) and MSB2 (right panel). The dashed lines represent Chamberlain models at different temperatures. The temperatures along with their corresponding density and χ^2 error estimate are included in the right-hand corner of each panel. The error bars represent the 1σ uncertainties.

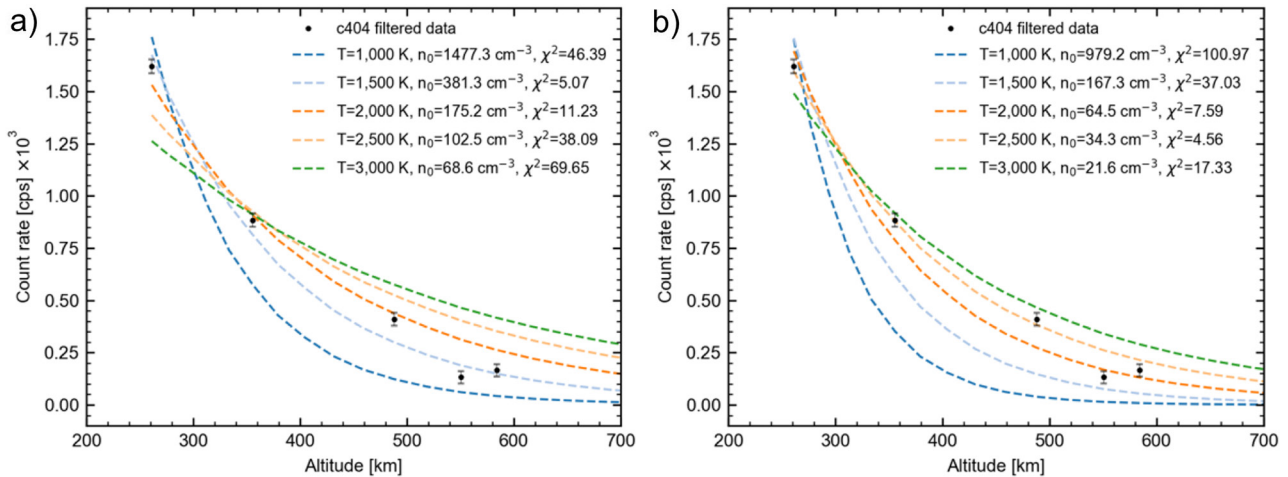


Figure 9. K (a) and Mn (b) Chamberlain model fits to low-altitude c404 data on the dawn side during MSB2. The dashed lines represent Chamberlain models at different temperatures. The temperatures along with their corresponding density and χ^2 error estimate are included in the right-hand corner of each panel. The error bars represent the 1σ uncertainties.

we were unable to fit our data with the temperatures reported for Al in Bida and Killen (2017). For each multiplet of K and Mn, we computed the g-value for each wavelength and then summed them (Table 3). For K, the best-fit was achieved for $n_0 = 381.3 \text{ cm}^{-3}$ and $T = 1,500 \text{ K}$ (Figure 9a). For Mn, the best-fit was achieved for $n_0 = 34.3 \text{ cm}^{-3}$ and $T = 2,500 \text{ K}$ (Figure 9b).

We also noticed that the parameters of the Chamberlain model deduced from the low-altitude data on the dawn side did not fit the low-altitude data on the nightside. However, it is very difficult to fit the c404 data on the nightside. It will be necessary to wait for the orbital phase to accumulate data on the night side.

6. Discussion and Conclusion

During both flybys, PHEBUS visible channels observed the exosphere of Mercury and detected multiple species, including Ca. The configuration of the flybys, associated with the geometry of observation, revealed a much extended Ca exosphere (beyond 10,000 km) on the morning side. This is surprising given the short photoionization lifetime of Ca (the lifetime varies from 23 min at perihelion to 52 min at aphelion, Burger et al., 2014): the atoms are very likely to be photoionized before reaching these high altitudes. This implies that the release process of neutral Ca in the exosphere of Mercury is very energetic or that recombination of Ca^+ ions, either by electron impact or charge exchange, could occur far from the surface. The process currently favored by the community is a two-step process where Ca is ejected from the surface in a molecular form that is subsequently dissociated (Killen et al., 2005). The primary source considered is micrometeoroid impact vaporization (Killen & Hahn, 2015). The process which dissociates the Ca-bearing molecules to produce energetic Ca atoms is still debated (Killen, 2016).

With the c422 channel low-altitude data on the morning side, we derived a large e-folding distance ($\sim 2,500\text{--}2,800 \text{ km}$), in agreement with previous studies (Burger et al., 2012; Vervack et al., 2010), and a high temperature ($>50,000 \text{ K}$), consistent with previous studies (Burger et al., 2012, 2014). Both the large e-folding distance and the high exobase temperature tend to confirm the energetic nature of exospheric Ca. However, the exobase temperature deduced from the low-altitude morning side data does not fit the predawn nightside data. This could indicate a day/night asymmetry with a source of Ca located predominantly on the dayside. Ca atoms observed on the nightside would then come mainly from the transport around the planet, with a significant proportion of them being photoionized before reaching the nightside. Alternatively, the day/night asymmetry could also be the consequence of a shift of the main source of Ca away from the dawn region. Pokorný et al. (2018) showed that micrometeoroid impact vaporization flux at $\text{TAA} = 240^\circ$ and $\text{TAA} = 300^\circ$ (encompassing the period of PHEBUS observations) peaked not exactly at 6 a.m. but between 7 and 8 a.m.

In future work, we aim to include the effect of photoionization and non-uniform distribution of Ca to model the Ca exosphere (Chaufray et al., 2023).

During both flybys, we also detected species with the c404 channel at low altitudes on the morning side. The bandwidth of the c404 detector is wide enough to allow the detection of the emission lines of Ca⁺, Al, and Mn, as well as those of K. It is therefore likely that we have detected at least one of these emission lines during both flybys, but it is impossible to identify the contribution of each species. Observations of Ca⁺ and Al with MESSENGER/MASCS (Vervack et al., 2016) show relatively flat profiles with altitude, which is not consistent with the profiles obtained using the c404 channel during both flybys that show an exponential decrease with altitude. On the other hand, ground-based observations of Al show profiles exponentially decreasing with altitude (Bida & Killen, 2017). Using the Chamberlain model, Bida and Killen (2017) derived a temperature between 6,000 and 8,000 K. However, this range of temperature is not consistent with the PHEBUS c404 profiles, ruling out Al as the species detected by the PHEBUS c404 channel.

In contrast with Al and Ca⁺ profiles, the Mn profile shows an exponential decrease (Vervack et al., 2016). The scale height we deduced from the MESSENGER observations (~100 km) is similar to the one we deduced from the c404 data (~135 km) but not the radiance at the surface (one order of magnitude difference). The location and timing of Mn detection in Mercury's exosphere by MESSENGER suggest a relationship with the comet Encke's dust trail (Vervack et al., 2016). We might then expect that its release is dominated by meteoroid impact vaporization. During impact events, Mn is produced mainly in the form of atoms. Thus, their temperature is assumed to be ~3,000 K that is, the typical temperature of the impact-produced cloud (Berezhnoy, 2018). The temperature we deduced with the Chamberlain model (~2,500 K) is consistent with the expected temperature of impact-produced Mn, but the TAA of the flybys does not match with the crossing of comet Encke's trail. Furthermore, the detections of Mn reported by Vervack et al. (2016) were made only toward the end of the mission, over a limited range of TAA and located in the predawn nightside region. The range of TAA does not match the TAA of BepiColombo flybys nor does the location of the species.

For potassium, we fitted a Chamberlain model to the c404 profile from the second flyby and estimated a temperature at an exobase of 1500 K. It is marginally compatible with recent results from Lierle et al. (2022) that revealed K to be the coldest metallic constituent of Mercury's exosphere. Their linewidth measurements indicate cold temperature, between the surface temperature (i.e., 700 K) and 1000 K. This temperature range favors thermal desorption or photodesorption as the dominant mechanism for K release, as sputtered or meteoroid-vaporized K would appear much hotter.

Finally, Lierle et al. (2022) deduced a disk-averaged brightness for the K doublet at 404 nm of 50 R. The spectra obtained during the observations described in Vervack et al. (2016) yield line-of-sight radiances of 25.5 R (Al 394.51 nm), 63.0 R (Al 396.26 nm), 82.4 R (Ca⁺ 393.48 nm), 41.2 R (Ca⁺ 396.96 nm) and average line-of-sight radiance for Mn of 80.4 R. The intensities observed with the PHEBUS c404 channel are rather of the order of ~1 kR. Even if we sum the contributions of all the species, we are far below the values observed by the PHEBUS c404 channel. To sum up, comparison with previous studies is inconclusive as to the species detected by the c404 channel during the flybys. We can only state that the scale height is quite low (~135 km) and that the temperature seems to be below 3,000 K.

Appendix A: Calibration of PHEBUS's Visible Channels

The effective area, corresponding to the instrument sensitivity, is the product of the entrance area by the spectral efficiency of the instrument (mirror, grating and detector). To retrieve the effective area of the visible channels c404 and c422, we have used the observations of different stars (Table A1), conducted with the slit across and a 1 s exposure time. As a star is a point source, we consider the following relation:

$$CR = A_{\text{eff}} F \quad (\text{A1})$$

With CR the count rate associated with the star and F the transmitted flux of the star on the channels. The transmitted flux F is expressed as

$$F = \int \phi(\lambda) T(\lambda) d\lambda \quad (\text{A2})$$

Where ϕ is the photometric flux of the star, T is the bandwidth of the visible channels and λ the wavelength. The photometric fluxes of the stars at multiple wavelengths were retrieved from Burnashev (1985). The spectral response of the visible channels was measured on ground with the slit across (Figures 6 and 7 in Quémerais et al. (2020)).

Table A1

Star Name, Hipparcos Identification (HIP id.), Observed Count Rate on c404 During Flip Maneuvers (CR_{404}), Transmitted Flux on c404 (F_{404}) and Its Deduced c404 Effective Area ($A_{\text{eff}404}$), Observed Count Rate on c422 During Flip Maneuvers (CR_{422}), Transmitted Flux on c422 (F_{422}) and Its Deduced c422 Effective Area ($A_{\text{eff}422}$)

Name	HIP id.	CR_{404} [ph.s ⁻¹]	F_{404} [ph.s ⁻¹ .cm ⁻²]	$A_{\text{eff}404} = CR_{404}/F_{404}$ [cm ²]	CR_{422} [ph.s ⁻¹]	F_{422} [ph.s ⁻¹ .cm ⁻²]	$A_{\text{eff}422} = CR_{422}/F_{422}$ [cm ²]
α Eridani *	7588	2,106	1.65×10^5	1.14×10^{-2}	1,367	2.08×10^5	5.48×10^{-3}
α Carinae	30438	5,006	4.99×10^5	9.57×10^{-3}	3,746	4.75×10^5	7.41×10^{-3}
ϵ Canis Majoris *†	33579	1,485	1.02×10^5	1.24×10^{-2}	999	8.37×10^4	9.20×10^{-3}
β Carinae *	45238	1,051	6.53×10^4	1.26×10^{-2}	889	5.90×10^4	1.12×10^{-2}
α Leonis *†	49669	1,516	1.09×10^5	1.19×10^{-2}	1,140	9.35×10^4	9.74×10^{-3}
α Crucis *†	60718	2,813	2.05×10^5	1.26×10^{-2}	1,936	1.69×10^5	1.01×10^{-2}
α Virginis *†	65474	2,116	1.70×10^5	1.11×10^{-2}	1,605	1.40×10^5	9.80×10^{-3}
β Centauri *†	68702	3,000	2.37×10^5	1.17×10^{-2}	2015	1.96×10^5	9.10×10^{-3}
α Aquilae *†	97649	1,642	1.24×10^5	1.14×10^{-2}	1,280	1.18×10^5	8.89×10^{-3}
α Pavonis†	100751	1,106	6.84×10^4	1.28×10^{-2}	841	5.82×10^4	1.05×10^{-2}
α Gruis *†	109268	1,131	7.32×10^4	1.23×10^{-2}	840	6.42×10^4	9.52×10^{-3}

Table A1 lists the stars identified during the flip observations, their names and Hipparcos identification number, the count rate observed on both detectors, along with the flux of the star transmitted on both channels and the effective area of both channels deduced from the measurements. The correction of the background includes only the dark current. The contribution of the zodiacal light is indeed negligible when the slit is across (about 5 counts per second). The dark current was measured during several observations at the parking position, where the entrance of the baffle is obstructed by the parking bracket, with the slit across and with an exposure time of 1 s. The mean dark current of c404 is equal to 228.5 ± 47.4 counts per second, while that of c422 is equal to 229.0 ± 47.1 counts per second.

For each channel, we compute the mean value of the effective area. We then consider only the values comprised within the $\pm 1\sigma$ range around the mean value previously calculated. The considered stars are marked with an asterisk in Table A1 for the c404 channel and with a Croce for the c422 channel. The effective area deduced for c404 is $1.19 \times 10^{-2} \pm 2.3 \times 10^{-4}$ cm² and for c422 $0.96 \times 10^{-2} \pm 2.8 \times 10^{-4}$ cm². The uncertainty on the effective area takes into account the uncertainty on the measurement, that is, the photon noise and the uncertainty related to the dark current.

Appendix B: Correction of the Background During Flybys

We notice that the background levels were much higher than the estimated value (based on observations made in cruise) and not constant (difference between the beginning and the end of the observation during both flybys for the c404 channel—Figure 3). The difference is even more pronounced on the second flyby. Therefore, we cannot simply remove a constant; we need to derive a background correction model specific to Mercury flybys.

Let C_{404} be the number of counts registered by the c404 channel and C_{422} be the number of counts registered by the c422 channel. They can be expressed as follows:

$$C_{404} = N_{404} + B_{404} + CT \times N_{422} \quad (\text{B1})$$

$$C_{422} = N_{422} + B_{422} \quad (\text{B2})$$

Where N_{422} is the number of counts attributed to calcium, B_{422} the number of counts attributed to the background of the c422 channel, N_{404} the number of counts attributed to the species detected by the c404 channel, B_{404} the number of counts attributed to the background of the c404 channel and CT the coefficient of Ca cross-talk. To model the transition from the mean value at the beginning of the flyby to the mean value at the end of the flyby, we use a sine function. Therefore, we model the background as follows:

$$B(x) = \begin{cases} b_1, & x < x_1 \\ b_1 + (b_2 - b_1) \times \sin^2\left(\frac{\pi}{2} \frac{(x-x_1)}{(x_2-x_1)}\right), & x_1 \leq x < x_2 \\ b_2, & x \geq x_2 \end{cases} \quad (\text{B3})$$

Where b_1 represents the number of counts to be removed from the start to index x_1 , b_2 represents the number of counts to be removed from index x_2 to the end. B_1 corresponds to the mean value of the number of counts registered by the c404 channel at the beginning of the flyby. The values for both flybys are given in Table B1. To derive b_2 , we consider the data at the end of the flyby. From a certain altitude h ($\sim 5,000$ km), the c404 channel no longer detects any species. Its signal is then the sum of two components:

$$C_{404} = B_{404} + CT \times N_{422} \quad (\text{B4})$$

Table B1
Parameters of the Background Correction for Both Flybys

Flyby n°	CT	b_1	b_2	x_1	x_2	ΔB
1	0.058	6,233	6,615	210	280	612
2	0.099	5,960	7188	125	160	787

Note. CT is the coefficient of the Ca cross-talk, b_1 is the number of counts to remove at the beginning of the flyby (before index x_1), b_2 is the number of counts to remove at the end of the flyby (after x_2) and ΔB is the average value of the difference between the number of counts registered by the c404 channel and those registered by the c422 channel over the first 30 points for MSB1, 75 first points for MSB2. b_1 is the average value of the number of counts registered by the c404 channel over the first 30 data points for MSB1, 75 first data points for MSB2.

At the beginning of each flyby, we notice a constant difference ΔB between the signals of the two detectors. No species are detected on this part of the flybys, so it is only the difference between the backgrounds of the two channels:

$$\Delta B = B_{404} - B_{422} \quad (\text{B5})$$

We assume that this difference remains the same throughout each flyby. Therefore, combining Equations B2, B4, and B5, we have

$$\begin{aligned} B_{404} + CT \times (C_{422} + \Delta B - B_{404}) \\ C_{404} = CT \times C_{422} + (1 - CT) \times B_{404} + CT \times \Delta B \\ \alpha \times C_{422} + \beta \end{aligned} \quad (\text{B6})$$

To derive α and β (and therefore CT and b_2), we perform a linear regression on the data for which the altitude is higher than h (i.e., $\sim 5,000$ km) after the closest approach. We then deduce b_2 :

$$b_2 = \frac{\beta - \alpha \times \Delta B}{1 - \alpha} \quad (\text{B7})$$

We then obtain the useful information (i.e., the signal related to the species):

$$C_{422_{\text{corr}}} = N_{422} = C_{422} - B + \Delta B \quad (\text{B8})$$

$$C_{404_{\text{corr}}} = N_{404} = C_{404} - B - CT \times C_{422_{\text{corr}}} \quad (\text{B9})$$

The values of b_1 , b_2 , CT, and ΔB are given in Table B1 for both flybys.

Appendix C: Uncertainties

The estimate of the goodness of fit χ^2 can be expressed as follows:

$$\chi^2 = \frac{1}{n} \sum_{i=1}^n \frac{(d_i - m_i)^2}{\sigma_i^2} \quad (C1)$$

where n is the total number of measurements, d_i are the data values measured with errors σ_i , and m_i are the modeled values. In Section 5.2, d_i corresponds to the count rate CR corrected for the background level:

$$CR = \frac{W - D}{\Delta t} \quad (C2)$$

With W the number of counts registered by the detector, D the dark current and Δt the exposure time. Based on the propagation of errors, the error associated with the measured count rate can be expressed as follows:

$$\sigma_{CR}^2 = \frac{1}{\Delta t^2} (\sigma_W^2 + \sigma_D^2) \quad (C3)$$

Because the visible channels are composed of a photomultiplier tube to detect photons, the number of counts registered by the visible channels does not correspond exactly to the number of incident photons. The relation between the number of counts W , the number of photons P and the dark current D is as follows:

$$W = kP + D \quad (C4)$$

The propagation of errors leads to the following relation:

$$\sigma_W^2 = k^2 \sigma_P^2 + \sigma_D^2 \quad (C5)$$

σ_P being the photon noise (i.e., $\sigma_P = \sqrt{P}$), we get:

$$\sigma_W^2 = k(W - D) + \sigma_D^2 \quad (C6)$$

We then get

$$\sigma_{CR}^2 = \frac{k}{\Delta t} CR + \frac{2}{\Delta t^2} \sigma_D^2 \quad (C7)$$

To derive the coefficient k , we performed a linear regression on the data obtained during different stellar observation campaigns. We assumed that the dark current is the same on both detectors (as well as its uncertainty). The coefficient k is nearly equal to 1 for both channels; therefore, we considered it equal to 1.

As for the modeled values, we combine Equations 1, 2, and 6 to get:

$$m_i = g \times N_i \times A_{\text{eff}} \times \Omega / (4\pi) \quad (C8)$$

with g the g -value of the species, N_i the line-of-sight column density associated with each measurement, A_{eff} the effective area of the detector and Ω the solid angle.

Data Availability Statement

The observation data of the visible channels of PHEBUS during the first two flybys of Mercury by BepiColombo used in the study are available at BepiColombo PHEBUS Team (2023).

Acknowledgments

The BepiColombo mission to explore Mercury is an international cooperation between the European Space Agency, ESA, and the Japan Aerospace Exploration Agency, JAXA. This work was supported by the CNES. It is based on observations with PHEBUS embarked on the BepiColombo/MPO mission.

References

BepiColombo PHEBUS Team. (2023). Observations of Mercury's exosphere with the visible channels of PHEBUS during the first two Mercury flybys with the BepiColombo mission (1.0). [Dataset]. LATMOS. Retrieved from http://doi.latmos.ipsl.fr/phebus-c404_c422-mercury-swingby_count_rate_latmos.html

Berezhnoy, A. A. (2018). Chemistry of impact events on Mercury. *Icarus*, 300, 210–222. <https://doi.org/10.1016/j.icarus.2017.08.034>

Bida, T. A., & Killen, R. M. (2011). Observations of Al, Fe, and Ca+ in Mercury's exosphere. In *EPSC-DPS Joint Meeting 2011* (Vol. 2011, p. 1621).

Bida, T. A., & Killen, R. M. (2017). Observations of the minor species Al and Fe in Mercury's exosphere. *Icarus*, 289, 227–238. <https://doi.org/10.1016/j.icarus.2016.10.019>

Bida, T. A., Killen, R. M., & Morgan, T. H. (2000). Discovery of calcium in Mercury's atmosphere. *Nature*, 404(6774), 159–161. <https://doi.org/10.1038/35004521>

Broadfoot, A. L., Shemansky, D. E., & Kumar, S. (1976). Mariner 10: Mercury atmosphere. *Geophysical Research Letters*, 3(10), 577–580. <https://doi.org/10.1029/GL003i010p00577>

Burger, M. H., Killen, R. M., McClintock, W. E., Merkel, A. W., Vervack, R. J., Cassidy, T. A., & Sarantos, M. (2014). Seasonal variations in Mercury's dayside calcium exosphere. *Icarus*, 238, 51–58. <https://doi.org/10.1016/j.icarus.2014.04.049>

Burger, M. H., Killen, R. M., McClintock, W. E., Vervack, R. J., Jr., Merkel, A. W., Sprague, A. L., & Sarantos, M. (2012). Modeling MESSENGER observations of calcium in Mercury's exosphere. *Journal of Geophysical Research*, 117(E12), E00L11. <https://doi.org/10.1029/2012JE004158>

Burnashev, V. I. (1985). Catalogue of data on energy distribution in spectra of stars in a uniform spectrophotometric system. *Abastumanskaia Astrofizicheskaia Observatoriia Byulleten*, 59, 83–89.

Chamberlain, J. W. (1963). Planetary coronae and atmospheric evaporation. *Planetary and Space Science*, 11(8), 901–960. [https://doi.org/10.1016/0032-0633\(63\)90122-3](https://doi.org/10.1016/0032-0633(63)90122-3)

Chassefière, E., Maria, J.-L., Goutail, J.-P., Quémerais, E., Leblanc, F., Okano, S., et al. (2010). PHEBUS: A double ultraviolet spectrometer to observe Mercury's exosphere. *Planetary and Space Science*, 58(1), 201–223. <https://doi.org/10.1016/j.pss.2008.05.018>

Chaufray, J.-Y., Leblanc, F., Robidel, R., Quémerais, E., & Koutroumpa, D. (2023). Simulation of the Ca emission at Mercury and comparison with the observations by PHEBUS/BepiColombo during the first two flybys (EGU23-6164). *EGU23. Copernicus Meetings*. <https://doi.org/10.5194/egusphere-egu23-6164>

Coddington, O. M., Richard, E. C., Harber, D., Pilewskie, P., Woods, T. N., Chance, K., et al. (2021). The TSIS-1 hybrid solar reference spectrum. *Geophysical Research Letters*, 48(12), e2020GL091709. <https://doi.org/10.1029/2020GL091709>

Killen, R. M. (2016). Pathways for energization of Ca in Mercury's exosphere. *Icarus*, 268, 32–36. <https://doi.org/10.1016/j.icarus.2015.12.035>

Killen, R. M., Bida, T. A., & Morgan, T. H. (2005). The calcium exosphere of Mercury. *Icarus*, 173(2), 300–311. <https://doi.org/10.1016/j.icarus.2004.08.022>

Killen, R. M., Burger, M. H., Vervack, R. J., & Cassidy, T. A. (2018). Understanding Mercury's exosphere: Models derived from MESSENGER observations. In B. J. Anderson, L. R. Nittler, & S. C. Solomon (Eds.), *Mercury: The view after MESSENGER* (pp. 407–429). Cambridge University Press. <https://doi.org/10.1017/9781316650684.016>

Killen, R. M., & Hahn, J. M. (2015). Impact vaporization as a possible source of Mercury's calcium exosphere. *Icarus*, 250, 230–237. <https://doi.org/10.1016/j.icarus.2014.11.035>

Kramida, A., Ralchenko, Y., & Reader, J., & NIST ASD Team. (2022). NIST atomic spectra database. <https://doi.org/10.18434/T4W30F>

Leinert, C., Bowyer, S., Haikala, L. K., Hanner, M. S., Hauser, M. G., Levasseur-Regourd, A.-C., et al. (1998). The 1997 reference of diffuse night sky brightness. *Astronomy & Astrophysics Supplement Series*, 127(1), 1–99. Article 1. <https://doi.org/10.1051/aas:1998105>

Lierle, P., Schmidt, C., Baumgardner, J., Moore, L., Bida, T., & Swindle, R. (2022). The spatial distribution and temperature of Mercury's potassium exosphere. *The Planetary Science Journal*, 3(4), 87. <https://doi.org/10.3847/PSJ/ac5c4d>

McClintock, W. E., Bradley, E. T., Vervack, R. J., Killen, R. M., Sprague, A. L., Izenberg, N. R., & Solomon, S. C. (2008). Mercury's exosphere: Observations during MESSENGER's first Mercury flyby. *Science*, 321(5885), 92–94. <https://doi.org/10.1126/science.1159467>

McClintock, W. E., Vervack, R. J., Bradley, E. T., Killen, R. M., Mouawad, N., Sprague, A. L., et al. (2009). MESSENGER observations of Mercury's exosphere: Detection of magnesium and distribution of constituents. *Science*, 324(5927), 610–613. <https://doi.org/10.1126/science.1172525>

Merkel, A. W., Cassidy, T. A., Vervack, R. J., McClintock, W. E., Sarantos, M., Burger, M. H., & Killen, R. M. (2017). Seasonal variations of Mercury's magnesium dayside exosphere from MESSENGER observations. *Icarus*, 281, 46–54. <https://doi.org/10.1016/j.icarus.2016.08.032>

Pokorný, P., Sarantos, M., & Janches, D. (2018). A comprehensive model of the meteoroid environment around Mercury. *The Astrophysical Journal*, 863(1), 31. <https://doi.org/10.3847/1538-4357/aad051>

Potter, A., & Morgan, T. (1985). Discovery of sodium in the atmosphere of Mercury. *Science*, 229(4714), 651–653. <https://doi.org/10.1126/science.229.4714.651>

Potter, A., & Morgan, T. (1986). Potassium in the atmosphere of Mercury. *Icarus*, 67(2), 336–340. [https://doi.org/10.1016/0019-1035\(86\)90113-2](https://doi.org/10.1016/0019-1035(86)90113-2)

Quémerais, E., Chaufray, J.-Y., Koutroumpa, D., Leblanc, F., Reberac, A., Lustremont, B., et al. (2020). PHEBUS on Bepi-Colombo: Post-launch update and instrument performance. *Space Science Reviews*, 216(4), 67. <https://doi.org/10.1007/s11214-020-00695-6>

Vervack, R. J., Killen, R. M., McClintock, W. E., Merkel, A. W., Burger, M. H., Cassidy, T. A., & Sarantos, M. (2016). New discoveries from MESSENGER and insights into Mercury's exosphere. *Geophysical Research Letters*, 43(22), 11545–11551. <https://doi.org/10.1002/2016GL071284>

Vervack, R. J., McClintock, W. E., Killen, R. M., Sprague, A. L., Anderson, B. J., Burger, M. H., et al. (2010). Mercury's complex exosphere: Results from MESSENGER's third flyby. *Science*, 329(5992), 672–675. <https://doi.org/10.1126/science.1188572>

Wurz, P., Fatemi, S., Galli, A., Halekas, J., Harada, Y., Jäggi, N., et al. (2022). Particles and photons as drivers for particle release from the surfaces of the Moon and Mercury. *Space Science Reviews*, 218(3), 10. <https://doi.org/10.1007/s11214-022-00875-6>